International Journal of Nanomedicine

Dovepress
Taylor & Francis Group

Open Access Full Text Article

ORIGINAL RESEARCH

Melittin-Loaded Fe_3O_4-Au_{shell} Nanocomposite Hydrogel for Multifunctional Treatment of Atopic Dermatitis

Wen Chao Xu[1–3,*], Xiao Qu Duan[2,*], Li Zhong[4,*], Yuan Chao Li[2], Lei Ran[2], Hai Huan Xu[3], Qian Wu[2], Ke Huang[2], Na Nan Miao[2], Tao Jiang[2], Qiu Han Chen[2], Yang Zhang[2], Hong Zhuang Zhang[5], Ru Peng Wang[2], Mingfu Gong[1]

[1]Department of Radiology, Xinqiao Hospital, Army Medical University, Chongqing, 400037, People's Republic of China; [2]Department of Rheumatology and Dermatology, Xinqiao Hospital, Army Medical University, Chongqing, 400037, People's Republic of China; [3]Department of Dermatology, Characteristic Medical center of Chinese People's Armed Police Force, Tianjin, 300162, People's Republic of China; [4]National & Local Joint Engineering Research Center of Harbour Oil & Gas Storage and Transportation Technology/Zhejiang Key Laboratory of Pollution Control for Port-Petrochemical Industry, Zhejiang Ocean University, Zhoushan, 316022, People's Republic of China; [5]Department of Burns, Characteristic Medical Center of Chinese People's Armed Police Force, Tianjin, 300162, People's Republic of China

*These authors contributed equally to this work

Correspondence: Mingfu Gong, Department of Radiology, Xinqiao Hospital, Army Medical University, 183 Xinqiao Main Street, Shapingba District, Chongqing, 400037, People's Republic of China, Email hummer198625@tmmu.cdu.cn; Ru Peng Wang, Department of Rheumatology and Dermatology, Xinqiao Hospital, Army Medical University, 183 Xinqiao Main Street, Shapingba District, Chongqing, 400037, People's Republic of China, Email Wrp71@tmmu.edu.cn

Background: Atopic dermatitis (AD) severely impairs the lives of patients and existing therapies are limited by side effects or insufficient efficacy. In this study, we developed a multifunctional nanocomposite hydrogel that integrates immunoregulation, antioxidant, antibacterial, and skin repair for the integrative treatment of AD.

Methods: Fe_3O_4-Au_{shell} (FA) nanoparticles (NPs) were synthesized, melittin (MLT) was anchored onto FA NPs, and MLT-Fe_3O_4-Au_{shell} (MFA) was loaded into Pluronic F-127 (PF127), to prepare the MFA@PF127 hydrogel. After a comprehensive evaluation of the physicochemical properties, MFA@PF127 was incubated with HaCaT cells and administered to AD lesions to demonstrate its therapeutic efficiency for AD in vitro and in vivo.

Results: The Fe_3O_4-Au_{shell} (FA) NPs with a heterodimer morphology and uniform size were successfully prepared, and the MLT was then loaded onto FA NPs with a high loading efficiency of 64.5%. By loading MLT-FA (MFA) NPs into PF127, the MFA@PF127 nanocomposite hydrogel with thermosensitivity, a porous structure, and good biocompatibility was successfully constructed. After incubation with MFA@PF127 and irradiated with near-infrared (NIR) laser, HaCaT cells showed significantly lower thymic stromal lymphopoietin (TSLP) expression and reactive oxygen species (ROS) levels than the control. The growth of *S. aureus* and biofilm formation were suppressed by MFA@PF127 under NIR irradiation. When administered to AD lesions, MFA@PF127+NIR significantly alleviated the dermatitis severity score; downregulated TSLP, IL-4, and IL-13 expression, suppressed *S. aureus* colonization; reduced ROS levels; and alleviated epidermal thickening and mast cell infiltration.

Conclusion: MFA@PF127 exhibited multifunctionality of immunoregulation, and antioxidant and antibacterial activities, which significantly alleviated AD symptoms in a mouse model and provided a potential strategy for AD treatment after further preclinical validation.

Keywords: nanoparticles, immunoregulation, antibacterial, photothermal therapy, ROS, pluronic F127

Introduction

Atopic dermatitis (AD) is a chronic inflammatory skin disorder that affects 15–20% of children and up to 10% of adults.[1] AD is characterized by xerosis, recurrent eczematous eruptions, and intense pruritus, all of which significantly impair patients' quality of life.[1,2] Many patients also develop psychological comorbidities and even suicidal ideation, resulting in substantial

https://doi.org/10.2147/IJN.S606172
Received: 11 March 2026
Accepted: 14 May 2026
Published: 9 June 2026

health and economic burdens on individuals, families, and society.[3,4] AD pathogenesis involves the interaction of Th2-cell hyperactivation, microbial dysbiosis, oxidative stress, and epidermal barrier dysfunction, which makes the clinical therapy challenged.[5,6] Topical corticosteroids are currently recommended as the first-line therapy because of their potent anti-inflammatory effects; however, long-term use of corticosteroids is associated with local adverse reactions, including hypertrichosis, striae, pigmentary changes, and telangiectasia.[7] Although novel biological agents can mitigate some of these side effects, their high cost, relatively narrow immunosuppressive targets, and relapse after discontinuation have collectively limited their clinical applicability.[8] In addition, most therapies target only a single pathological pathway, hardly breaking the pathological self-perpetuating vicious cycle of AD, and often result in suboptimal outcomes. Thus, innovative therapeutic strategies that can comprehensively regulate the complex pathological network of AD are urgently required.

Melittin (MLT), the principal active component of honeybee venom, has been investigated for the treatment of various inflammatory diseases because of its significant immunomodulatory activity.[9–12] MLT also exhibits potent antibacterial activity against a range of pathogens, making it a highly effective natural antimicrobial peptide.[13,14] Additionally, MLT has been proven to effectively regulate organismic redox homeostasis by scavenging reactive oxygen species (ROS) and upregulating the expression and activity of key antioxidant enzymes.[15,16] However, dose-dependent and non-specific cytotoxicity severely limits the clinical application of MLT.[17] Combining MLT with other treatments based on the combination therapy strategy may reduce the dosage while maintaining therapeutic outcomes and mitigating adverse effects, thereby offering a new, feasible pathway for its clinical translation.[9]

Gold (Au) nanoparticles (NPs) exhibit high surface plasmon resonance (SPR), efficiently absorbing and converting light energy into heat, which enables precise photothermal therapy (PTT) at infection sites to effectively inhibit pathogen proliferation.[18] Notably, by modulating the morphology and size of Au NPs, their absorption peak and photothermal conversion efficiency can be controlled, thereby significantly enhance PTT efficacy.[19] Hollow-structured Au NPs, which exhibit stronger absorption in the near-infrared (NIR) region, are considered ideal materials for PTT.[20,21] Furthermore, Au NPs exert anti-inflammatory effects by regulating immune cell polarization, inhibiting the release of inflammatory cytokines, and blocking the NF-κB pathway.[22,23] As one of the earliest and most extensively studied iron-based nanozyme, iron oxide (Fe_3O_4) NPs can regulate oxidative stress by switchable enzyme-like activities in different microenvironments.[24] Thus, the Fe_3O_4-Au_{shell} heterodimer NPs integrating Fe_3O_4 with Au_{shell} were considered to be multifunctional of efficient immunoregulation, antioxidant, and antibacterial. More importantly, the metal-oxygen and metal-metal interactions between the Fe_3O_4 and Au_{shell} can enhance electron transfer, thereby potentially improving overall efficiency.[25] Therefore, we hypothesized that combining the Fe_3O_4-Au_{shell} with MLT could produce combined effects that target the complex pathological network of AD at a lower dosage.

Restoring skin barrier function is crucial for AD treatment. Hydrogels are widely used in skin wound repair because of their good tissue adhesion, moisturizing capacity, breathability, and excellent biocompatibility.[26–28] Pluronic F127 (PF127) hydrogel is a thermosensitive material that forms a stable gel at body temperature.[29,30] This hydrogel has a three-dimensional (3D) porous structure that enables sustained drug release, reduces adverse effects caused by local drug accumulation, and lowers the dosing frequency. Furthermore, PF127 possesses a high water content and skin-similar mechanical properties, providing a relatively enclosed, moist, and clean microenvironment for healing.

Herein, we proposed a novel multifunctional nanocomposite hydrogel MLT-Fe_3O_4-Au_{shell}@PF127 (MFA@PF127) which was composed of heterodimer Fe_3O_4-Au_{shell}, MLT and thermosensitive PF127, and was expected to be of excellent biocompatibility, immunomodulatory, antioxidant, and antibacterial activities (Scheme 1). After physicochemical characterization and In vitro evaluation, the nanocomposite hydrogel was further administrated to AD mice, to evaluate the multifunctionality and high efficiency and explore the feasibility of MFA@PF127 as a potential clinical strategy for AD treatment.

Materials and Methods

Materials

1-Octadecene (ODE) was purchased from Acros (Shanghai, China). Chloroauric acid ($HAuCl_4$), oleic acid (OA), Pluronic® F-127, and 1-chloro-2,4-dinitrobenzene (DNCB) were purchased from Sigma-Aldrich (Shanghai China). Iron pentacarbonyl ($Fe(CO)_5$) was purchased from New Dingpengfei Technology Development Co. Ltd. (Beijing, China). Trisodium citrate

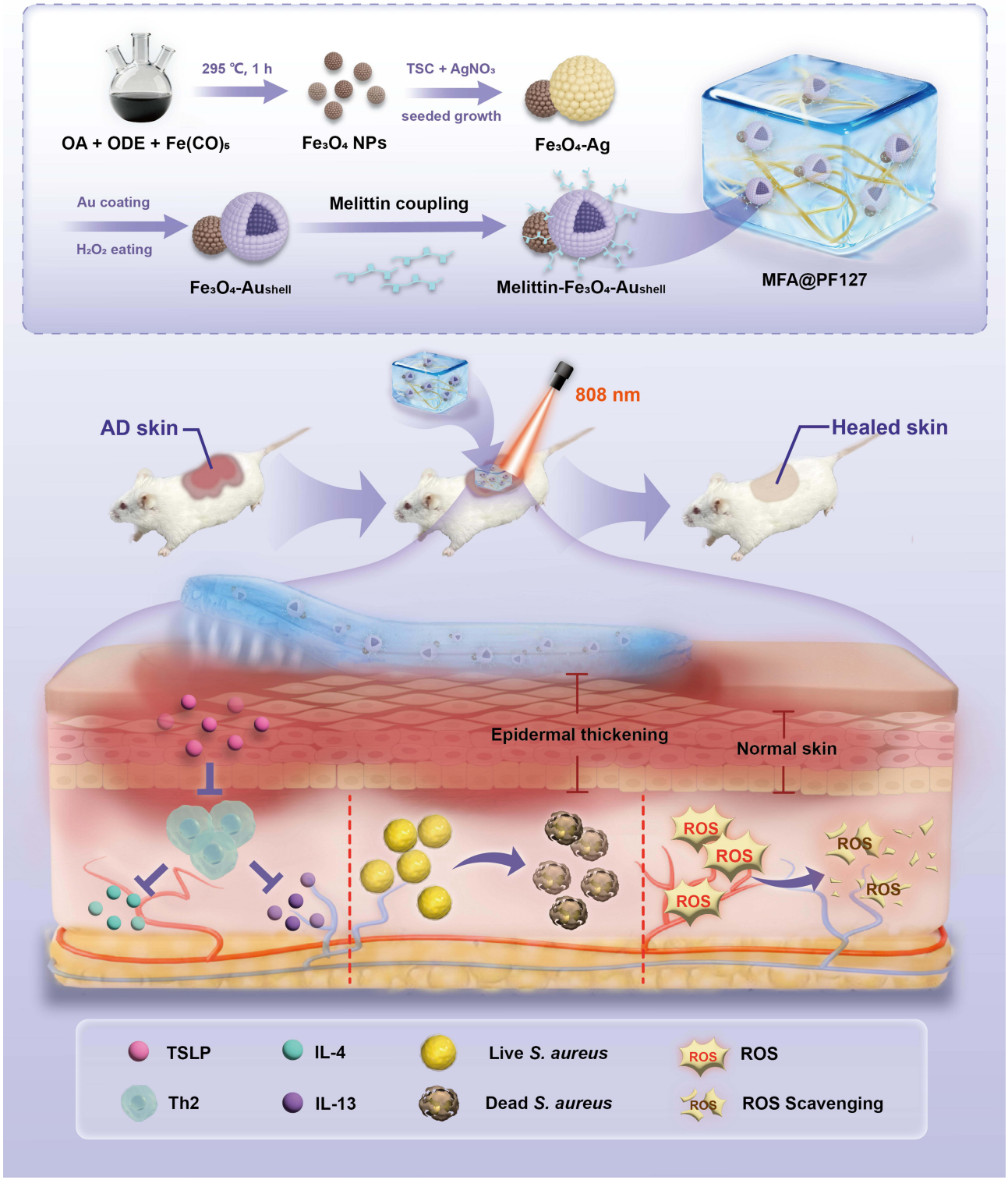

Scheme 1 Synthesis of the MFA@PF127 nanocomposite hydrogel and its combined therapeutic mechanism for AD.

https://doi.org/10.2147/IJN.S606172

(TSC) was purchased from Wokai Biotechnology Co. Ltd. (Beijing, China). Tetramethylammonium hydroxide (TMAH), silver nitrate ($AgNO_3$) and hydroxylamine hydrochloride ($NH_2OH{\cdot}HCl$) were purchased from Adamas-beta (Shanghai, China). Acetone was purchased from Aladdin (Shanghai, China). Dulbecco's modified Eagle's medium (DMEM), 0.25% trypsin-EDTA, fetal bovine serum (FBS), tumor necrosis factor-alpha (TNF-α), and interferon-gamma (IFN-γ) were purchased from Gibco (Shanghai, China). Melittin (MLT) was purchased from AbMole (Shanghai, China). Cell counting kit-8 (CCK-8) and bertani (LB) agar plates were purchased from BNCC (Beijing, China). The ROS, cell viability/cytotoxicity, and live/dead bacterial viability assay kits were purchased from Beyotime (Shanghai, China). Crystal violet was purchased from SolarBio (Beijing, China). Interleukin-4 (IL-4) and IL-13 enzyme-linked immunosorbent assay (ELISA) kits were obtained from ElabScience (Wuhan, China). TSLP antibody was purchased from Servicebio (Wuhan, China).

Synthesis of Fe_3O_4 NPs

20 mL ODE and 1.6 mL OA were mixed and stirred at 100 °C for 30 min under nitrogen atmosphere. Subsequently, 0.4 mL of $Fe(CO)_5$ was injected and the mixture was further heated to 295 °C. One hour later, the dispersion was cooled to room temperature, washed with acetone, and centrifuged (8500 rpm for 10 min). The precipitate was further purified via ethanol washing and centrifugation (8500 rpm for 10 min) and ultrasonically dispersed in a 10% TMAH solution to endow the prepared Fe_3O_4 NPs with hydrophilicity. After another centrifugation (10000 rpm for 10 min), the precipitate was finally dispersed in 20 mL ultrapure water and stored at 4 °C.

Synthesis of Fe_3O_4-Ag_{seed} NPs

40 mL ultrapure water, 1 mL Fe_3O_4 dispersion, and 1 mL TSC (1%, w/v) were mixed and heated to 60 °C with stirring. Subsequently, 500 μL of $AgNO_3$ solution (0.17%, w/v) was slowly added, followed by a 2 h reaction. The mixture was then cooled to room temperature and irradiated with 254 nm ultraviolet (UV) light for 0.5 h to mature the Ag seeds. After the addition of 4 mL TSC, 3.75 mL $AgNO_3$ solution was added dropwise over 1 h at 60 °C, followed by further heating for 0.5 h to prepare Fe_3O_4-Ag_{seed} NPs.

Synthesis of Fe_3O_4-Ag NPs

5 mL of the Fe_3O_4-Ag_{seed} dispersion, 6.4 mL TSC and 80 mL of deionized water were mixed, and the mixture was heated to 60 °C under magnetic stirring. Then, 2.8 mL $AgNO_3$ solution was added dropwise over 3 h. After the reaction was complete, the mixture was centrifuged to obtain Fe_3O_4-Ag NPs.

Synthesis of Fe_3O_4-Au_{shell} NPs

Fe_3O_4-Au_{Shell} NPs were synthesized based on galvanic replacement chemistry.[31] Briefly, 5 mL of the Fe_3O_4-Ag dispersion was mixed with 6.25 mM hydroxylamine hydrochloride solution under magnetic stirring. Subsequently, 5 mL of a 0.465 mM $HAuCl_4$ solution was added within 12.5 min. After the color of the solution stabilized, 150 μL H_2O_2 (30%, w/v) was added and the mixture was stirred for 2 h. Finally, the Fe_3O_4-Au_{shell} NPs were stored at 4 °C.

Preparation of MLT-Fe_3O_4-Au_{shell}

Owing to its abundant surface charge, MLT was loaded onto the FA NPs through electrostatic adsorption in the present study. Briefly, 5 mL of the FA dispersion was mixed with 50, 100, and 200 μL of MLT (1 μg/μL) solutions and shaken at 150 rpm for 30 min at room temperature. After ultrafiltration and centrifugation for 30 min, the precipitate was re-suspended in ultrapure water. The residual MLT content in the supernatant was measured using a bicinchoninic acid (BCA) protein assay kit, and the MLT loading efficiency of the FA-NPs was calculated. The MLT-Fe_3O_4-Au_{shell} dispersion was then frozen at −80 °C for 24 h and lyophilized (Coolsafe 110, Labogene, Denmark) for storage at 4 °C.

Preparation of MFA@PF127

The phase transition temperature and gelation time of PF127 are usually influenced greatly by the concentration, and the concentration was set at 25% to make the PF127 be body temperature sensitive in this study.[32,33] Briefly, 2.5 g of PF127

was first dissolved in 7.5 mL precooled PBS in ice bath with stirring, followed by the addition of MFA to prepare the MFA@PF127 nanocomposite hydrogel with Au concentration of 500 μg/mL and MLT concentration of 100 μg/mL, and finally the hydrogel was stored at 4 °C. FA@PF127 and MLT@PF127 hydrogels were prepared following the same procedure, with an Au concentration of 500 μg/mL or MLT concentration of 100 μg/mL.

Characterization

The morphology and size distribution of the NPs and hydrogel were observed by transmission electron microscopy (TEM; HT7700, Hitachi, Japan) and scanning electron microscopy (SEM; CLARA, TESCAN, Czechia). The elemental distribution of the NPs was characterized by energy-dispersive X-ray spectroscopy (EDS, Tecnai G2 F30, FEI, USA). The elemental content of the NPs was determined by inductively coupled plasma optical emission spectrometry (ICP-OES; Thermo Fisher Scientific, USA). The absorption spectra were measured using a UV-visible (UV-vis) spectrophotometer (L6S, Shanghai, China). The zeta potential was determined using a zeta potential analyzer (Z3000, NICOMP, USA).

MFA Release Evaluation

2 mL MFA@PF127 hydrogel solution was placed in a 37 °C water bath for 5 min, followed by the addition of 3.0 mL PBS. The mixture was then shaken (150 rpm) at 37 °C. At predetermined time intervals (0.5, 1, 2, 4, 6, 8, 10, 12, 24, and 48 h), 1 mL of the supernatant was withdrawn and an equal volume of PBS was added to maintain a constant total volume. Because MLT was stably conjugated to the FA NP surface, they were considered to be of similar release kinetics, and the released MFA was determined by quantifying the released Au_{shell} with ICP-OES. The released MLT calculated based on its loading efficiency and the quantified Au_{shell} concentration.

Cell Culture

HaCaT (human immortalized keratinocytes) cells were purchased from CELLCOOK (Shanghai, China). The cells were cultured in complete DMEM (CDMEM) containing 10% FBS and 1% penicillin-streptomycin in a humidified incubator at 37 °C with 5% CO_2. When the cells reached approximately 80% confluence, they were detached using 0.25% trypsin-EDTA and subcultured at a 1:3 ratio. All subsequent experiments were conducted with cells in the logarithmic growth phase.

Cytocompatibility and Cell Uptake

Cytocompatibility was assessed using the CCK-8 assay. First, certain volumes of sterilized MLT@PF127 hydrogel were soaked in CDMEM (the final concentrations of MLT: 1.25, 2.5, 5, 10, and 20 μg/mL) for 24 h to prepare extracts which were labeled as $MLT_{1.25\mu g}$ @PF127, $MLT_{2.5\mu g}$@PF127, $MLT_{5\mu g}$@PF127, $MLT_{10\mu g}$ @PF127, $MLT_{20\mu g}$@PF127. HaCaT cells were seeded in 96-well plates at a density of 3×10^3 cells/well. After attachment, the medium was replaced with 100 μL of the corresponding extract, whereas that of the control group was replaced with fresh CDMEM, and the cells were cultured for an additional 48 h. Subsequently, the extracts were discarded, the cells were washed thrice with PBS, and 100 μL of fresh medium containing 10 μL CCK-8 solution was added to each well. After 2 h of incubation, absorbance was measured at 450 nm using a microplate reader (BK-EL10A, BIOBASE, China). To determine the safe concentration of MLT, the cytotoxicity of PF127, MLT@PF127, FA@PF127, and MFA@PF127 were further evaluated using the same method (the concentrations of MLT and Au were maintained at 10 μg/mL and 50 μg/mL, respectively, and these conditions were used for all subsequent experiments unless otherwise stated). The cytocompatibility of PF127, MLT@PF127, FA@PF127, and MFA@PF127 was visually assessed using calcein-AM/PI staining. Following a 48 h co-culture of HaCaT cells with the respective extracts in 24-well plates, the cells were stained and observed under an inverted fluorescence microscope (IX73, Olympus, Japan). To evaluate NP uptake, HaCaT cells were incubated with the MFA@PF127 extract for 2 h and then observed using TEM.

In vitro Immunoregulation and Antioxidant Activity

For the immunoregulation determination, HaCaT cells were stimulated with recombinant human TNF-α/IFN-γ (20 ng/mL) to establish an inflammatory cell model.[34] In brief, the HaCaT cells were seeded in 6-well plates at a density of 2×10^5 cells/

well. When the confluence reached 80%, the medium was replaced with 2 mL of fresh CDMEM, CDMEM containing TNF-α/IFN-γ, MLT@PF127 extract containing TNF-α/IFN-γ, FA@PF127 extract containing TNF-α/IFN-γ, or MFA@PF127 extract containing TNF-α/IFN-γ. 6 h later, the cells in a 6-well plate were used for RT-qPCR to determine the TSLP mRNA levels. After 6 h, the supernatants of the cells cultured in another 6-well plate were collected for TSLP protein measurement using ELISA (The detailed RT-qPCR and ELISA methods were provided in the Supplementary Methods 1).

The antioxidant efficacy of the hydrogel was assessed using a H_2O_2-induced oxidative stress model.[35] The media of HaCaT cells in 6-well plates were discarded after 80% confluence and replaced with 2 mL fresh CDMEM containing H_2O_2 (500 μM), MLT@PF127 extract containing H_2O_2 (500 μM), FA@PF127 extract containing H_2O_2 (500 μM), and MFA@PF127 extract containing H_2O_2 (500 μM). After 6 h, cells were collected and resuspended in serum-free medium containing 10 μM CM-H_2DCFDA. After light-protected incubation at 37 °C for 20 min, the fluorescence intensity was quantified by flow cytometry (Gallios, Beckman Coulter, USA).

Photothermal Performance

To evaluate the photothermal performance, 500 μL of the MFA@PF127 hydrogel was placed in a 1.5 mL centrifuge tube and irradiated with an 808-nm NIR laser at different power densities (0.5, 0.75, 1.0, and 1.25 W/cm^2), and the real-time temperature was monitored using a thermal imaging camera. Additionally, the photothermal stability was assessed by performing four consecutive laser on-off cycles (heating and cooling).

In vitro Antibacterial and Antibiofilm Activity

S. aureus (ATCC6538) was used to evaluate the antibacterial activity of MFA@PF127. Sterilized hydrogels (200 μL of PF127, MLT@PF127, FA@PF127, or MFA@PF127) were placed in 24-well plates. After hydrogel gelation, 200 μL of bacterial suspension (1×10^6 CFU/mL) and 1 mL of LB broth were added to each well, and the plates were incubated at 37 °C for 6 h, the Bacterial suspensions without any addition served as the control. The FA@PF127 and MFA@PF127 groups were irradiated with an 808-nm NIR laser (1.25 W/cm^2) for 10 min before incubation. Afterwards, the bacterial suspension was collected, and its optical density at 600 nm (OD_{600}) was measured using a microplate reader. The bacterial suspension was then diluted and 100 μL of the suspension was spread on LB agar plates. After 24 h of culture, colonies were photographed and quantified. To visualize bacterial viability, the bacterial suspensions were stained with DMAO and PI and observed using a multifunctional microplate imaging system (Apx100, Olympus, Japan). Treated bacteria were fixed and observed using SEM.

To further evaluate the antibiofilm properties, bacterial suspensions (10^6 CFU/mL) were co-cultured with PF127, MLT@PF127, FA@PF127, and MFA@PF127 extracts (MLT: 20 μg/mL, Au:100 μg/mL), and the bacterial suspension co-cultured with an equal volume of PBS served as the control. After 48 h, biofilms were fixed and stained with crystal violet for 30 min. The bound crystal violet was dissolved in absolute ethanol, and the OD_{590} was quantified using a microplate reader.

Animal Experiments

The AD mouse model was established following a previous study.[36] All animals used in this study were female BALB/c mice aged 6 weeks, purchased from Vital River (Beijing, China). After acclimatization for 1 week, 25 mice were randomly selected for model establishment, and five mice were used as controls. One day prior to model establishment, a dorsal region (approximately 2.5×3.5 cm) was depilated. Two hundred microliters of 1% (w/v) DNCB solution (dissolved in acetone: olive oil at 3:1 v/v) was applied to the dorsum three times weekly, followed by 1 week incubation. From day 14 onward, 200 μL of 0.5% DNCB solution was applied every day for a week followed by the application of 1% DNCB solution every day for a week, and 200 μL of 0.5% DNCB solution was applied daily for 3 days. After successful establishment of the AD model, the mice were randomly treated with PF127, MLT@PF127, FA@PF127+NIR, or MFA@PF127+NIR (n=5) from day 31 onward, and 5 mice untreated mice served as controls. The treated mice received 1 mL of the corresponding hydrogel on their lesions daily for 1 week. For the FA@PF127+NIR and MFA@PF127+NIR groups, an additional 10 min of 808 nm laser irradiation was applied following hydrogel administration. DNCB (0.5%) was applied every other day throughout the treatment period. Body weight and dermatitis severity

scores of the mice were monitored throughout the study. The dermatitis severity score was calculated as the sum of the scores (0, none; 1, mild; 2, moderate; 3, severe) for the four key symptoms of AD: erythema/hemorrhage, scarring/dryness, edema, and excoriation/erosion. Dermatitis scoring was recorded by two trained investigators independently once weekly at the same day until the mice were sacrificed. If any discrepancy was observed, the investigators would re-evaluate the symptoms together and reached a final score. The total dermatitis severity score for each mouse was then calculated by summing the four individual symptom scores.

After euthanized on day 38 major organs and dorsal skin tissues of all the mice were collected for histopathological examination including H&E, toluidine blue, and immunofluorescence, and blood samples were harvested for the alanine transaminase (ALT), aspartate transaminase (AST), blood urea nitrogen (BUN), and creatinine (CREA) determination. All the stained sections were reviewed and analyzed by two pathologists independently in a blinded manner and an agreement was reached by re-evaluating together if there was any disagreement. After homogenization of skin tissues, the levels of IL-4 and IL-13 were measured by ELISA (Supplementary Methods 2). The skin tissues were digested to prepare single-cell suspensions, and then stained with the CM-H_2DCFDA probe to evaluate the in vivo antioxidant effect of the hydrogel.

The *S.aureus* colonization model in mouse skin was established according to a previously reported method.[6] In brief, after being immersed in the *S. aureus* suspension with a concentration of 1×10^6 CFU/mL for 5 minutes, the gauzes were applied to the skin lesions of AD mice on day 28 and removed after 24 h. On day 31, the colonized *S.aureus* were collected using a sterile swab by wiping the lesion surface 10 times before treatment. Then, the bacteria on the swab were then suspended in sterile PBS and finally spread on LB agar plates. On day 38, the *S.aureus* colonization was assessed again following the same method.

Statistical Analysis

All experiments were independently repeated 3–5 times. Data are presented as mean ± standard deviation (SD). Comparisons among multiple groups were performed using one-way analysis of variance (ANOVA), followed by Tukey's post hoc test for all pairwise comparisons. All statistical analyses were conducted using GraphPad Prism software (version 10.5.0). $P < 0.05$ was considered statistically significant.

Results and Discussion

Synthesis and Characterization of MFA@PF127

FA NPs were prepared according to our previously reported protocol,[37] as illustrated in Scheme 1. First, Fe_3O_4 NPs were synthesized via thermal decomposition of $Fe(CO)_5$. TEM characterization (Figure 1A) revealed that the synthesized NPs were nearly spherical, uniform in size, and monodisperse, with an average diameter of 10.9 ± 0.6 nm (Figure S1). Subsequently, Ag^+ ions were reduced and deposited onto the Fe_3O_4 surface through the synergistic reduction of Fe^{2+} and TSC. After the seeded growth, an Fe_3O_4-Ag heterodimer with a typical "dumbbell" morphology was successfully synthesized (Figure 1B). According to the galvanic replacement principle, Au^{3+} is reduced to Au^0 on the Fe_3O_4-Ag template in the presence of $NH_2OH{\cdot}HCl$, forming a Ag@Au core-shell nanostructure. After etching the Ag core with H_2O_2, the desired Fe_3O_4-Au_{shell} heterodimer NPs were produced (Figure 1C). Analysis of 100 particles revealed that the Au_{shell} NPs possessed an outer diameter of 14.3 ± 1.9 nm and an inner diameter of 9.3 ± 1.5 nm (Figure 1D and Figure S2), with a relatively narrow size distribution.

Because of the SPR phenomenon, the absorption spectra of Au NPs are highly dependent on their morphology and size.[19] Solid Au nanospheres typically exhibit an absorption peak at 520 nm.[38] In contrast, Au_{shell} nanostructures absorb light at longer wavelengths, and their absorption peak shows a distinct red-shift with increasing inner-to-outer diameter ratio.[20,21] Therefore, the synthesis of Au_{shell} NPs was further confirmed by monitoring changes in the spectrum. As shown in Figure 1E, with the addition of the Au precursor, the characteristic absorption peak of the spherical Ag NPs at 396 nm gradually decreases and exhibits a red shift. Following the addition of 2 mL chloroauric acid, a broad absorption band with a peak at 736 nm emerged, confirming the formation of the Au_{shell} structure. Given the broad NIR absorption profile and high absorption efficiency, an 808 nm laser was selected for subsequent photothermal experiments. EDS elemental mapping

 https://doi.org/10.2147/IJN.S606172

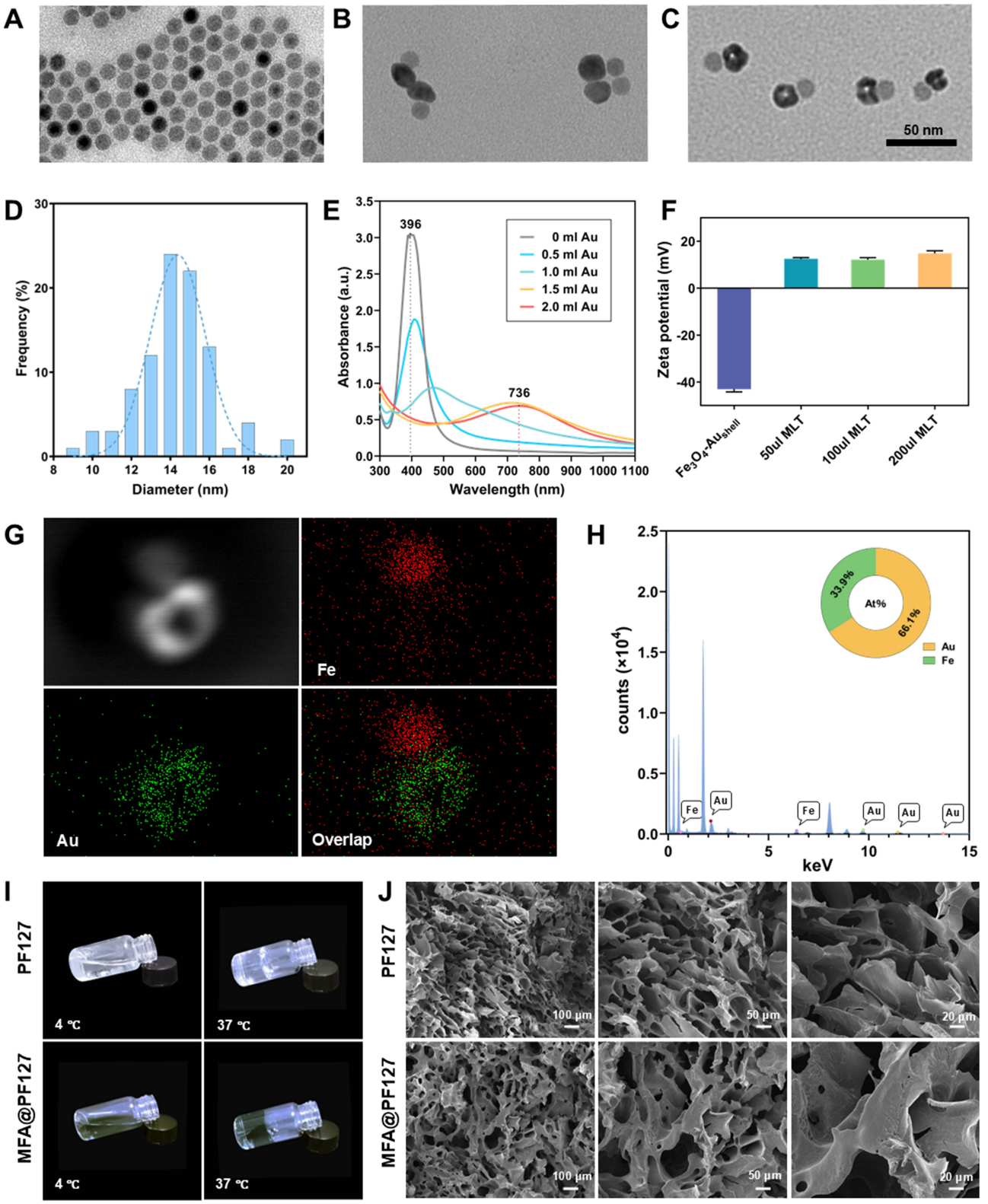

Figure 1 Characterization of the MFA@PF127 nanocomposite hydrogel. (**A**–**C**) TEM images of the Fe_3O_4, Fe_3O_4-Ag, and Fe_3O_4-Au_{shell} NPs. (**D**) Size distribution of the outer diameter of Au_{shell} NPs. (**E**) UV-vis absorption spectra of Fe_3O_4-Ag, Fe_3O_4-Ag@Au, and Fe_3O_4-Au_{shell} NPs. (**F**) Zeta potential of Fe_3O_4-Au_{shell} NPs before and after MLT loading. (**G** and **H**) EDS elemental mapping and composition analysis of Fe_3O_4-Au_{shell} NPs. (**I**) Photographs of PF127 and MFA@PF127 hydrogels at 4 °C and 37 °C. (**J**) SEM images of the PF127 and MFA@PF127 hydrogels.

(Figure 1G) confirmed that the Fe signals were localized on one side of the NPs in a solid spherical pattern, whereas the Au signals were distributed on the opposite side in a hollow shell pattern. The elemental percentages of Fe and Au were 33.9% and 66.1%, respectively (Figure 1H). ICP showed that the Au and Fe concentrations were 203.8 μg/mL and 62.5 μg/mL of the NPs dispersion, respectively. The zeta potential of −43.0 ± 1.2 mV of the synthesized NPs confirmed their excellent colloidal stability (Figure 1F). These results demonstrate that dumbbell-shaped NPs, consisting of solid iron oxide and hollow Au NPs, were successfully synthesized and exhibited excellent stability in aqueous systems.

Owing to the abundant surface charges, MLT was loaded onto the surface of Fe_3O_4-Au_{shell} NPs via strong electrostatic interactions. After MLT conjugation, the zeta potential changed from −43.0 ± 1.2 mV to 14.9 ± 1.1 mV, confirming the successful loading of MLT onto the surface of Fe_3O_4-Au_{shell} NPs (Figure 1F). The successful loading of MLT was further confirmed by the BCA assay, and its loading efficiency (LE) was calculated to be 63–64.5% when the MLT concentration was varied.

To fabricate a thermosensitive hydrogel in response to body temperature and to ensure that the loaded functional components could be efficiently released, MFA NPs were dispersed into the PF127 hydrogel to prepare the MFA@PF127 nanocomposite hydrogel. As shown in Figure 1I, MFA@PF127 exhibited thermosensitivity comparable to that of pure PF127, which remained liquid at 4 °C and formed a stable gel at 37 °C. SEM (Figure 1J) further revealed that MFA@PF127 had a similar 3D structure to of PF127, which was porous and beneficial for absorbing wound exudate, enabling sustained drug release and facilitating gas and tissue fluid exchange during the healing process. The release of MFA from the hydrogel was further evaluated by ICP-OES. As shown in Figure S3, MFA@PF127 exhibited a relatively steady release profile, with MFA being continuously released from the hydrogel over 48 h, achieving a cumulative release of 96.4%, demonstrating its sustained-release property. These results confirmed the successful construction of the MFA@PF127 nanocomposite hydrogel, which integrated favorable thermosensitive responsiveness and efficient MLT loading with a sustained-release capability.

In vitro Cytocompatibility and Cellular Uptake

To determine the optimal concentration of the MLT@PF127 hydrogel, its cytocompatibility was evaluated using a CCK-8 assay. As shown in Figure 2D, when cells were incubated with MLT@PF127 hydrogel extracts at concentrations ≤10 μg/mL for 48 h, the cell viability was not significantly different from that of the control group. As the concentration increased, the cell viability began to decline, which may be attributed to the dose-dependent cytotoxicity of MLT. Therefore, $MLT_{10\mu g}$@PF127 was selected for the subsequent experiments. CCK-8 assay further verified the cytocompatibility of PF127, MLT@PF127, FA@PF127, and MFA@PF127. As shown in Figure 2E, after 48 h of treatment with the various hydrogel extracts, all cells maintained good viability, and their relative cell viability remained above 87%, suggesting that the prepared hydrogels exhibited no obvious cytotoxicity. The biocompatibility of these hydrogels was visually confirmed by live/dead cell staining (Figure 2G). After 48 h of incubation, most cells exhibited regular and spread morphology, showing green fluorescence with minimal red fluorescence, indicating that the majority of the cells were viable. These results demonstrated the cytocompatibility of the designed MFA@PF127 nanocomposite hydrogel.

The efficient internalization of NPs by HaCaT cells is a prerequisite for their synergistic therapeutic effects. Therefore, we evaluated the cellular uptake of MFA by HaCaT cells. After 2 h of incubation with the MFA@PF127 extract, a small number of NPs adhered to the cell membrane surface, and numerous dumbbell-shaped NPs with solid and hollow structures were observed inside the cells (Figure 2A and B). The morphology and size of all intracellular NPs were similar to those shown in Figure 1C, indicating that the internalized NPs were Fe_3O_4-Au_{shell} NPs. Previous studies have presented similar results and concluded that NPs without any targeting ligand are usually internalized into cells via caveolin-mediated endocytosis or macropinocytosis and subsequently enclosed within phagocytic vesicles in the cytoplasm.[39] Notably, no NPs were observed within the cell nucleus, suggesting that Fe_3O_4-Au_{shell} NPs have negligible genotoxicity (Figure 2C).

In vitro Immunoregulation and Antioxidant Activity

Excessive activation of Th2 cells is crucial for the onset and progression of AD, therefore, inhibiting Th2 activation is considered an effective strategy to significantly alleviate AD progression.[40] Typically, Th2 cells are activated by cytokines,

 https://doi.org/10.2147/IJN.S606172

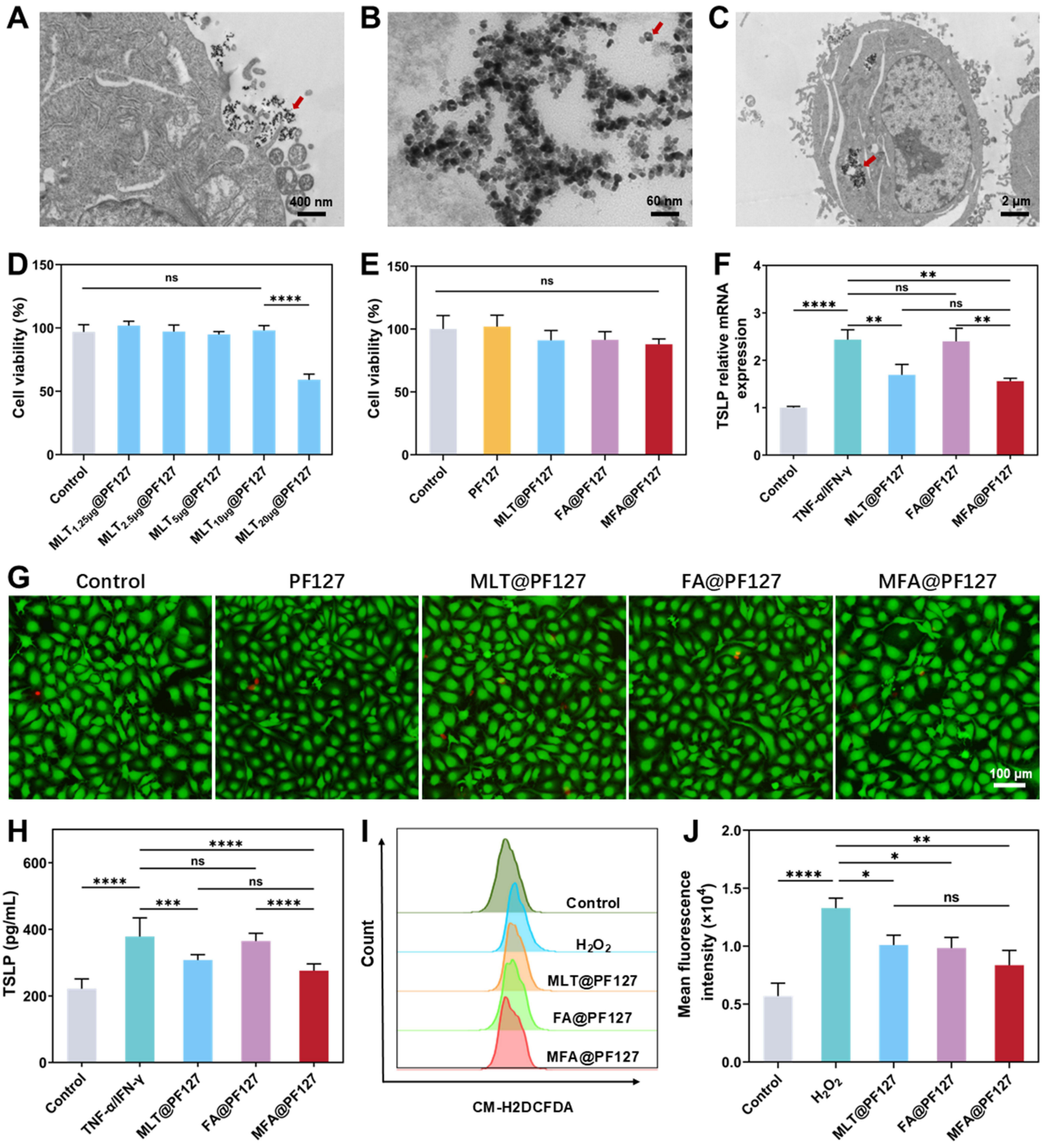

Figure 2 Evaluation of the cellular uptake, cytocompatibility, immunomodulatory function, and antioxidant activity of the MFA@PF127 nanocomposite hydrogel. (**A**–**C**) TEM images of HaCaT cells (Red arrows indicate the NPs). (**D**) Cell viability of HaCaT cells after 48 h of incubation with MLT@PF127 hydrogel extracts at different MLT concentrations. (**E**) Cell viability of HaCaT cells treated with different hydrogel extracts at 48 h. (**F**) Relative TSLP mRNA expression and TSLP protein secretion in HaCaT cells after different treatments. (**G**) live/dead fluorescence images of HaCaT cells after 48 h of incubation with different hydrogel extracts. Green: live cells; red: dead cells. (**H**) Protein secretion levels of TSLP in HaCaT cells under different treatment conditions. (**I** and **J**) Representative flow cytometry analysis of ROS levels and statistical graph. Data are presented as the mean ± SD (n = 3). **p* < 0.05, ***p* < 0.01, ****p* < 0.001, *****p* < 0.0001; ns indicates no significant difference.

such as TSLP, IL-1β, IL-25, and IL-33, among which TSLP often acts as a dominant driver.[41,42] Upon activation of the NF-κB signaling pathway in keratinocytes, TSLP gene transcription is upregulated,[43] which in turn induces the differentiation of naive $CD4^+$T cells into Th2 cells. Therefore, it can be hypothesized that type 2 immune responses are alleviated by downregulation of TSLP expression in keratinocytes. MLT and Au NPs have been demonstrated to possess significant

immunomodulatory activity and can suppress the release of inflammatory cytokines by inhibiting the NF-κB pathway.[9,10,22,23] Reasonably, the hypothesis that loading MLT onto Au NPs can significantly downregulate TSLP expression combinedly can be further drawn. Our results supported this hypothesis. Compared with control cells, HaCaT cells stimulated with TNF-α/IFN-γ showed significantly upregulated TSLP mRNA expression (Figure 2F) ($p < 0.0001$), indicating the successful establishment of the cellular inflammation model. When co-incubated with FA@PF127, inflamed HaCaT cells showed a slight downward trend in TSLP mRNA expression, suggesting a mild immunomodulatory effect of FA. After co-incubation with MLT@PF127 and MFA@PF127, the elevated TSLP mRNA levels in inflamed HaCaT cells were remarkably reversed, with the MFA@PF127 group exhibiting the most significant downregulation of TSLP mRNA expression ($p < 0.01$). These results demonstrate the potent immunoregulatory activity of MLT and suggest the FA NPs may enhance the suppression of TSLP expression. The immunomodulatory effects of the prepared hydrogels were confirmed using ELISA. As shown in Figure 2H, TSLP levels were significantly upregulated by TNF-α/IFN-γ stimulation and then progressively reduced by FA@PF127, MLT@PF127, and MFA@PF127 treatments, which was consistent with the PCR results and further demonstrated the favorable immunomodulatory effect of MFA@PF127.

ROS not only directly damages keratinocytes and the skin barrier but also exacerbates inflammation by activating pathways such as NF-κB, promoting the expression of pro-inflammatory factors.[44,45] Therefore, reducing intracellular ROS levels is critical for relieving AD development and progression. Owing to the high ROS-regulating efficiency of MLT, Fe_3O_4 and Au NPs, the MFA NPs were integrated into the composite hydrogel to scavenge the ROS within the AD lesion.[16,24,46] After stimulation with H_2O_2, the cells showed significantly higher fluorescence intensity than the control group (Figure 2I and J) ($p < 0.0001$). When treated with MLT@PF127 or FA@PF127 extracts, intracellular ROS levels decreased to similar levels, but were significantly lower in the positive control cells ($p < 0.05$). Notably, the cells treated with MFA@PF127 exhibited the lowest ROS levels ($p < 0.01$). The great ROS scavenging of the composite hydrogel may originate from MLT, Au_{shell} and Fe_3O_4 NPs. MLT has been demonstrated to restore redox homeostasis in the body by activating the Nrf2/HO-1 pathway and enhancing the expression of key antioxidant enzymes.[15,16] In the neutral or weakly alkaline microenvironment of AD lesions, Fe_3O_4 and Au NPs usually exhibit catalase-like activity, which can efficiently catalyze the decomposition of hydrogen peroxide into water and oxygen under neutral conditions.[24,46,47]

Photothermal Properties

Because PTT was proposed as a combined antibacterial strategy in this study, the photothermal performance of the MFA@PF127 hydrogel was evaluated. Under 808 nm laser irradiation, the temperature of the hydrogel exhibited a power density- and time-dependent increase (Figure 3A and B). As the power density increased from 0.5 to 0.75, 1.0, and 1.25 W/cm^2, the corresponding peak temperatures were 38.0 °C, 46.8 °C, 50.5 °C, and 52.9 °C, respectively. The time required to reach these peak temperatures decreased progressively from 9.5 to 8.5, 6.5, and 6.0 min, indicating adequate photothermal performance of MFA@PF127. Because efficient bacterial eradication requires temperatures exceeding 50 °C for enough time, so a power density of 1.25 W/cm^2 was used in subsequent experiments, which can reach the desired temperature in the shortest time to ensure sufficient bactericidal duration.[48] The photothermal stability of the hydrogel was further evaluated through four on-off cycles. No significant temperature attenuation was observed, confirming the excellent photothermal stability of MFA@PF127 (Figure 3C). This stability suggests that MFA@PF127 maintains its effective antibacterial efficacy over repeated irradiation cycles.

In vitro Antibacterial and Antibiofilm Activity

S. aureus colonization is regarded as a key pathogenic factor in AD development and progression. After colonizing AD lesion, *S. aureus* secretes abundant superantigens that induce excessive Th2 cell activation and subsequent overproduction of inflammatory factors, ultimately exacerbating the inflammatory cascade and perpetuating the chronicity of AD.[13] Studies have indicated that approximately 70% of AD patients have *S. aureus* colonization in their lesion sites.[49] Therefore, antibacterial intervention represents an effective strategy to alleviate AD. MLT has demonstrated significant antibacterial activity.[13,14] Benefiting from the excellent photothermal properties of Au_{shell} NPs, FA enables rapid local temperature elevation under NIR irradiation, achieving efficient bacterial eradication through PTT.[18,19] Capitalizing on these complementary advantages, the synthesized MFA@PF127 hydrogel is expected to exhibit synergistic antibacterial

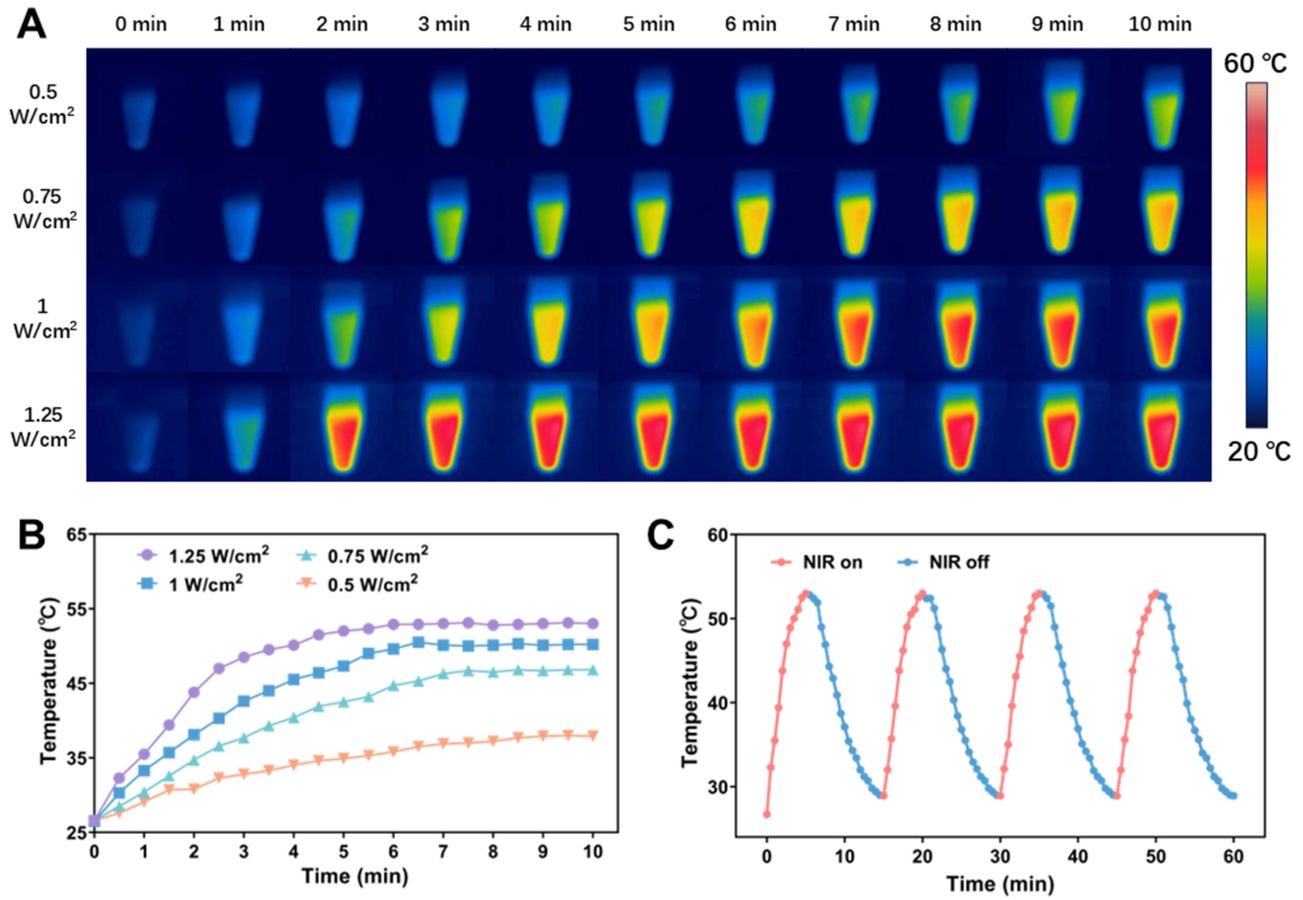

Figure 3 Photothermal performance of the MFA@PF127 nanocomposite hydrogel. (**A** and **B**) Real-time thermal images and temperature-time curves of MFA@PF127 hydrogel irradiated with an 808 nm NIR laser for 10 min at different power densities. (**C**) Temperature-time curve of MFA@PF127 hydrogel during four on-off cycles of 808 nm laser irradiation (1.25 W/cm^2).

effects through multiple mechanisms, enabling the highly efficient elimination of bacteria colonized in AD lesions. After 6 h of co-culture with the hydrogels, the bacterial suspensions in the control and PF127 groups were markedly more turbid than those in the other groups (Figure S4). Quantitative analysis via OD_{600} measurements further confirmed that the MFA@PF127+NIR group displayed the lowest OD_{600} values, whereas the OD_{600} of the FA@PF127+NIR, MLT@PF127, PF127, and control groups increased gradually (Figure S5). A plate colony counting experiment on the treated bacteria showed similar results. After spreading on LB agar plates and incubating for 24 h, the control and PF127 groups showed the densest colonies, whereas the colony counts in the MLT@PF127, FA@PF127+NIR, and MFA@PF127+NIR groups gradually decreased (Figure 4A). To further assess bacterial viability, live/dead fluorescence staining was performed (Figure 4B and E). Among all the groups, the most viable bacteria were found in the control and PF127, whereas the live bacteria decreased gradually in the MLT@PF127, FA@PF127+NIR and MFA@PF127+ NIR groups. SEM further revealed the morphological changes in the treated bacteria (Figure 4C). Control and PF127 treated bacteria exhibited intact and smooth surfaces without any obvious structural damage. The other three groups showed varying degrees of bacterial dissolution, with MFA@PF127+NIR-treated bacteria displaying disorganized surface structures and severe morphological changes.

Biofilms typically serve as protective barriers for colonizing bacteria, compromising their antibacterial and therapeutic efficacy against AD.[50,51] Therefore, antibiofilm can enhance the antibacterial effect and contribute to AD treatment. As shown in Figure 4D, the biofilms in the control and PF127 groups were intact and stained deep purple. The MLT@PF127 and FA@PF127+NIR groups showed reduced purple staining and partial structural damage in the biofilm, whereas the biofilm in the MFA@PF127+NIR group showed the least staining. These results were further confirmed

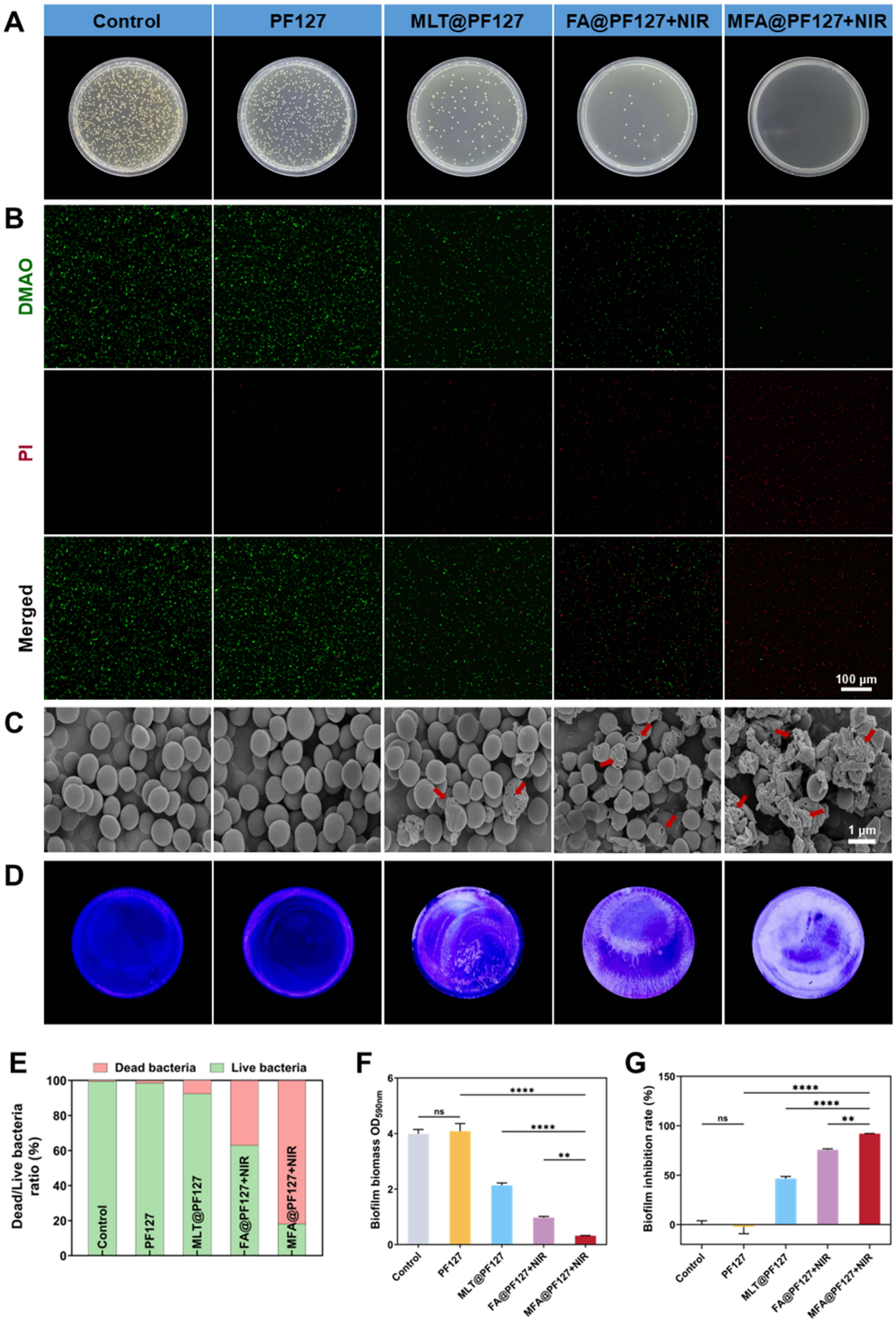

Figure 4 Antibacterial and antibiofilm activity of the MFA@PF127 nanocomposite hydrogel against *S. aureus*. (**A**) Representative images of bacterial colony growth on LB agar plates. (**B**) Representative live/dead bacterial staining images. (DMAO, a green-fluorescence dye, labels live bacteria, while PI, a red-fluorescence dye, labels dead bacteria). (**C**) SEM images of *S. aureus* morphology. (The red arrows indicate shrunk, deformed, or lysed *S. aureus*). (**D**) Representative images of crystal violet-stained *S. aureus* biofilms. (**E**) Quantitative analysis of the live/dead bacterial ratio based on DMAO/PI fluorescence staining. (**F**) Absorbance at 590 nm of ethanol-dissolved residual crystal violet from biofilm staining. (**G**) Inhibition rates of *S. aureus* biofilm formation. Data are presented as the mean ± SD (n = 3). $^{**}p < 0.01$, $^{****}p < 0.0001$; ns indicates no significant difference.

https://doi.org/10.2147/IJN.S606172

quantitatively after dissolving the crystal violet-bound dye in absolute ethanol, which showed a gradual decrease in absorbance (4.0, 4.1, 2.1, 1.0, and 0.3) and increased biofilm inhibition rates (0, −2.2, 46.6, 75.6%, and 92%) in the control, PF127, MLT@PF127, FA@PF127+NIR, and MFA@PF127+NIR groups (Figure 4F and G), indicating a significant combined inhibitory effect between MLT and FA-induced PTT on *S. aureus* biofilm formation. The optimal antibacterial properties of the MFA@PF127 hydrogel are expected to be reasonable. Studies have demonstrated that MLT possesses significant antibacterial efficacy, and PTT has emerged as a novel antibacterial strategy.[52,53] When combining MLT and PTT, improved antibacterial activity was observed. The phenomenon may result from the following mechanism. It is known that bacteria possess robust cell envelope structures, which not only hinder the penetration of foreign substances into bacteria but also confer them considerable tolerance to PTT. After treatment with MLT, numerous pores were created in the bacterial envelope.[54] The channels not only induce massive leakage of intracellular contents, leading to bacterial death, but also establishes "highways" for NP internalization. Consequently, when accumulating around the bacteria with numerous channels, the FA NPs may efficiently penetrate the bacterial interior, enabling effective ablation of the sensitized bacteria with lower temperature and shorter duration under NIR irradiation, and eradicating *S. aureus* efficiently with a Trojan horse-like strategy.

In vivo Therapeutic Efficacy

The experimental timeline is shown in Figure 5A. On day 31, mice in the model group exhibited obvious AD-like symptoms, including erythema, hemorrhage, scaling, and frequent scratching, indicating successful establishment of the DNCB-induced AD model. After seven days of treatment, all treated groups exhibited improvement in AD-like symptoms compared to the AD model group, and the MFA@PF127+NIR group mice showed the most prominent skin lesion recovery among all groups (Figure 5B). Visual observations were further validated using the dermatitis severity scores. Epidermal damage in the PF127 group (5.0 ± 1.0) showed no significant improvement compared with that in the AD group (6.4 ± 1.1). In contrast, both MLT@PF127 (2.0 ± 0.7) and FA@PF127+NIR (2.6 ± 0.9) treatments ameliorated skin damage, and the MFA@PF127+NIR-treated mice exhibited the lowest dermatitis score (0.8 ± 0.8), indicating the enhanced improvement of MLT and FA for epidermal damage (Figure 5C).

Epidermal thickening is one of the major pathological features of AD, and the quantification of epidermal thickness in treated mice was usually used for the therapeutic effect evaluation of the corresponding strategy. After histopathological analysis, we found that treatments with PF127, MLT@PF127, FA@PF127+NIR, and MFA@PF127+NIR all alleviated epidermal thickness, showing a decreasing trend in thickness (87.8 ± 11.2, 79.64 ± 9.0, 53.9 ± 8.5, and 17.1 ± 3.6 μm, respectively). The MFA@PF127+NIR group exhibited the thinnest epidermis, indicating a superior therapeutic efficacy against AD (Figure 5D and F).

Aberrant activation of the type 2 immune response is regarded as the core pathogenic mechanism in AD, characterized by Th2 cell activation and the subsequent release of IL-4 and IL-13 and the activation of mast cells.[41] Consequently, we further analyzed mast cell infiltration and IL-4 and IL-13 expression in the treated mice. As shown in Figure 5E and G, all treatment groups exhibited significant improvement in mast cell infiltration. PF127 treatment resulted in mild reduction. Both MLT@PF127 and FA@PF127+NIR treatments showed a greater reduction in mast cell infiltration, with superior efficacy compared with PF127. Most notably, MFA@PF127+NIR exhibited the lowest infiltration level (50.3 ± 3.1 cells/mm^2). Similar trends were observed for IL-4 and IL-13 levels (Figure 6C and D). Although cytokine concentrations following MFA@PF127+NIR treatment remained higher than those of the controls, they were significantly reduced compared with those in the AD model. The results of mast cell infiltration and IL-4/IL-13 secretion collectively demonstrate the immunoregulatory effects of MFA@PF127 on Th2 cells. Given the regulatory role of TSLP in Th2 cell function and the modulatory activity of MLT and Au NPs on TSLP, we determined the TSLP levels in all mice. Fluorescence staining (Figure 6A) revealed that the TSLP fluorescence intensity in the skin tissue of AD mice was significantly enhanced compared with that in the normal group, which was markedly reversed after MFA@PF127+NIR treatment (Figure 6B). These results indicated that the MFA@PF127+NIR regulated Th2 overactivation by blocking TSLP expression, thereby alleviating AD symptoms. As an important immune organ, spleen size is regarded as an objective indicator for assessing the immune status of the body. We found that the spleens of the model group mice were noticeably enlarged compared to those of the control group mice, suggesting immune hyperactivation in AD mice, possibly associated with Th2 cell-mediated

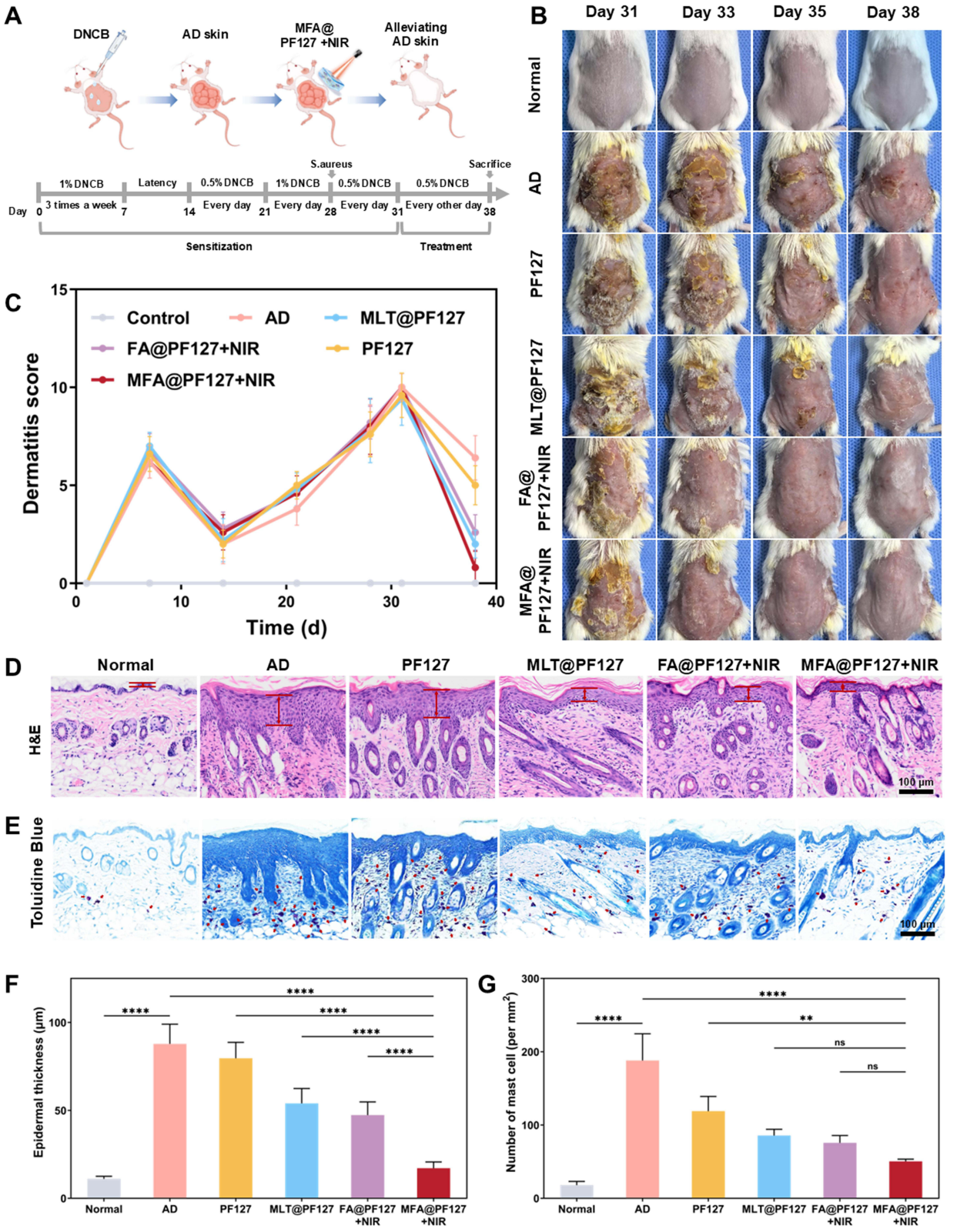

Figure 5 In vivo therapeutic effects of the MFA@PF127. (**A**) Schematic timeline for establishing the AD mouse model and the treatment protocol. (**B**) Representative photographs of dorsal skin lesions. (**C**) Dermatitis severity scores of the mice (n = 5). (**D**) H&E staining of mouse skin (n = 5) (Red double headed arrows indicate epidermal thickness). (**E**) Toluidine blue staining of mouse skin (n = 5) (Red arrows indicate mast cells). (**F**) Quantitative analysis of epidermal thickness based on the H&E staining (n = 5). (**G**) Statistical results of mast cell numbers (n = 5). Data are presented as mean ± SD. $^{**}p < 0.01$, $^{****}p < 0.0001$; ns indicates no significant difference.

https://doi.org/10.2147/IJN.S606172

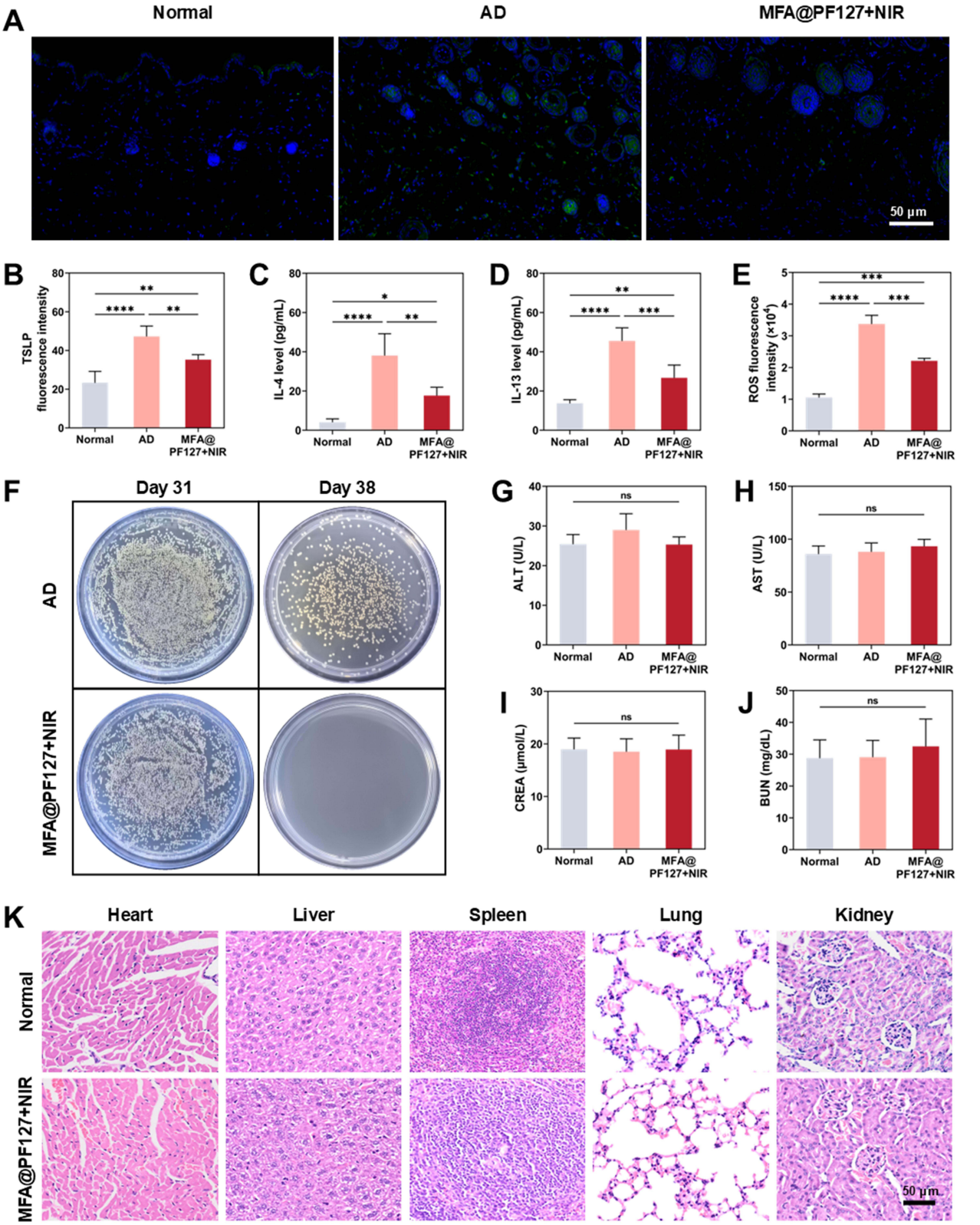

Figure 6 In vivo immunomodulatory efficacy and biosafety assessment of the MFA@PF127. (**A** and **B**) Representative immunofluorescence staining images of TSLP and the statistical analysis of the average TSLP fluorescence intensity in mouse skin (n = 5). (**C** and **D**) Expression levels of IL-4, IL-13 in skin measured by ELISA (n = 5). (**E**) Quantitative analysis of ROS fluorescence intensity in skin. (**F**) Representative photographs of bacterial cultured on LB agar plates. (**G**–**J**) Liver function (ALT and AST) and renal function (UREA and BUN) examinations (n = 3). (**K**) H&E staining of the heart, liver, spleen, lung, and kidney. Data are presented as the mean ± SD. *$p < 0.05$, **$p < 0.01$, ***$p < 0.001$, ****$p < 0.0001$; ns indicates no significant difference.

https://doi.org/10.2147/IJN.S606172

inflammation. Spleen index analysis further indicated various degrees of recovery in the treatment groups (9.1 ± 0.5, 6.7 ± 0.7, 5.4 ± 0.6, 5.2 ± 0.4, and 4.6 ± 0.3, respectively) compared to the model group, demonstrating the immunomodulatory efficacy of the MFA@PF127 hydrogel (Figure S6).

The antibacterial efficacy and ROS-scavenging activity of MFA@PF127 were validated in vivo. As shown in Figure 6F, after MFA@PF127+NIR treatment for seven days, *S. aureus* in the lesions was almost completely eradicated, whereas abundant *S. aureus* colonies were found within the lesions of untreated mice. Figure 6E shows the in vivo antioxidant effect of the composite nanogel, showing that the CM-H_2DCFDA fluorescence intensity in the MFA@PF127+NIR group was significantly lower than that in the model group. Together, these results indicate that MFA@PF127 not only eliminated *S. aureus* but also mitigated oxidative stress damage by scavenging excess ROS, thereby exerting a combined effect in the treatment of AD.

H&E staining of major organs and serum liver and kidney function analyses were performed to evaluate the in vivo biosafety of MFA@PF127. The tissue structures of the heart, liver, spleen, lungs, and kidneys in the treated groups remained intact and clear, with no pathological changes such as fibrosis, cellular degeneration, necrosis, or abnormal inflammatory cell infiltration (Figure 6K). The biochemical indicators of liver and kidney function in MFA@PF127-treated mice, including ALT, AST, BUN, and CREA, were not significantly different from those in the control group and remained within normal reference ranges (Figure 6G–J). These results indicate that the MFA@PF127 hydrogel exhibited good biocompatibility and safety in vivo.

Conclusions

In this study, we successfully synthesized a multifunctional composite nanohydrogel, MFA@PF127, by synthesizing dumbbell-shaped FA NP, anchoring MLT onto the FA surface based on electrostatic adsorption, and loading MFA into PF127. The hydrogel exhibited good biocompatibility both in vitro and in vivo, along with favorable immunomodulatory, antibacterial, and antioxidant activities. However, the present study has limitations. A 7-days treatment period and limited sample size were insufficient for the systematic assessment of the therapeutic effect and biosafety of MFA@PF127. Therefore, future studies with larger sample size and extended observation period have been proposed to further validate the therapeutic effect, long-term safety, and clinical-translation potential of MFA@PF127. In summary, the present study demonstrated the multifunctionality of MFA@PF127 nanocomposite hydrogel for AD treatment and provided a promising potential strategy for clinical therapy of AD.

Abbreviations

AD, atopic dermatitis; MLT, melittin; FA, Fe_3O_4 - Au_{shell}; MFA, melittin-Fe_3O_4-Au_{shell}; NPs, nanoparticles; PF127, pluronic F-127; PTT, photothermal therapy; ROS, reactive oxygen species; SPR, surface plasmon resonance; NIR, near-infrared; SEM, scanning electron microscopy; TEM, transmission electron microscopy; EDS, energy-dispersive X-ray spectroscopy; ICP-OES, inductively coupled plasma optical emission spectrometry; UV-vis, ultraviolet-visible spectroscopy; 3D, three-dimensional; BCA, bicinchoninic acid; ODE, 1-octadecene; $HAuCl_4$, chloroauric acid; OA, oleic acid; TSC, Trisodium citrate; $AgNO_3$, silver nitrate; $NH_2OH{\cdot}HCl$, hydroxylamine hydrochloride; TNF-α, tumor necrosis factor-alpha, IFN-γ, interferon-gamma; TMAH, Tetramethylammonium hydroxide; LE, loading efficiency; ALT, alanine transaminase; AST, aspartate transaminase; BUN, blood urea nitrogen; CREA, creatinine.

Ethics Approval

All experimental animal procedures were approved by the Animal Ethics Committee of Army Medical University (Approval No. AMUWEC20255367; Approval Date: June 10, 2025). The care and use of animals were performed in accordance with the Guidelines for the ethical review of laboratory animal welfare of People's Republic of China (GB/T 35892-2018), Guidelines for euthanasia of laboratory animal of People's Republic of China (GB/T 39760-2021) and American Veterinary Medical Association (AVMA) Guidelines for the Euthanasia of Animals. All mice were housed in a specific pathogen-free (SPF) environment. All experimental procedures were performed in strict accordance with the 3R principles, and every effort was made to minimize pain and distress. For procedures requiring anesthesia, mice were anesthetized with isoflurane inhalation in oxygen. Euthanasia was performed in accordance with relevant regulations. Specifically, mice were euthanized by continuous

inhalation of high-concentration isoflurane until respiratory and cardiac arrest occurred. To ensure irreversible death, cervical dislocation was performed immediately after the cessation of vital signs.

Acknowledgments

We acknowledge the use of FigDraw for figure illustration, and GraphPad Prism for chart creation.

Author Contributions

All authors made a significant contribution to the work reported, whether that is in the conception, study design, execution, acquisition of data, analysis and interpretation, or in all these areas; took part in drafting, revising or critically reviewing the article; gave final approval of the version to be published; have agreed on the journal to which the article has been submitted; and agree to be accountable for all aspects of the work.

Funding

This work was sponsored by the Chongqing Young and Middle-aged Medical High-end Talent Project (Mingfu Gong), Natural Science Foundation of Chongqing, China (CSTB2025NSCQ-GPX0587), and Young Doctoral Talent Incubation Project of the Second Affiliated Hospital of the Army Medical University (2023YQB034).

Disclosure

The authors declare no competing interests in this work.

References

1. Ständer S, Ropper AH. Atopic Dermatitis. *N Engl J Med*. 2021;384(12):1136–1143. doi:10.1056/NEJMra2023911
2. Kahn D, Iturriaga C, Bertran K, et al. Sleep quality in children with atopic dermatitis during flares and after treatment. *Sleep Sci*. 2020;13 (2):172–175. doi:10.5935/1984-0063.20190139
3. Brunner PM, Silverberg JI, Guttman-Yassky E, et al. Increasing Comorbidities Suggest that Atopic Dermatitis Is a Systemic Disorder. *J Invest Dermatol*. 2017;137(1):8–25. doi:10.1016/j.jid.2016.08.022
4. Filanovsky MG, Pootongkam S, Tamburro JE, et al. The Financial and Emotional Impact of Atopic Dermatitis on Children and Their Families. *J Pediatr*. 2016;169:284–290.e5. doi:10.1016/j.jpeds.2015.10.077
5. Ren Z, Silverberg JI. Association of Atopic Dermatitis With Bacterial, Fungal, Viral, and Sexually Transmitted Skin Infections. *Dermat Contact Atopic Occup Drug*. 2020;31(2):157–164. doi:10.1097/DER.0000000000000526
6. Jia Y, Hu J, An K, et al. Hydrogel dressing integrating FAK inhibition and ROS scavenging for mechano-chemical treatment of atopic dermatitis. *Nat Commun*. 2023;14:2478. doi:10.1038/s41467-023-38209-x
7. Coondoo A, Phiske M, Verma S, Lahiri K. Side-effects of topical steroids: a long overdue revisit. *Indian Dermatol Online J*. 2014;5(4):416–425. doi:10.4103/2229-5178.142483
8. Bangert C, Rindler K, Krausgruber T, et al. Persistence of mature dendritic cells, T_H 2A, and Tc2 cells characterize clinically resolved atopic dermatitis under IL-4Rα blockade. *Sci Immunol*. 2021;6(55):eabe2749. doi:10.1126/sciimmunol.abe2749
9. Zheng L, Zhan F, Jinxin L, et al. Melittin-Carrying Nanoparticle Suppress T Cell-Driven Immunity in a Murine Allergic Dermatitis Model. *Adv Sci Weinh Baden-Wurtt Ger*. 2023;10(7). doi:10.1002/advs.202204184
10. Liu L, Deng D, Li C, et al. The combination of modified acupuncture needle and melittin hydrogel as a novel therapeutic approach for rheumatoid arthritis treatment. *J Nanobiotechnology*. 2024;22(1):432. doi:10.1186/s12951-024-02722-y
11. Vu HD, Huynh PT, Ryu J, et al. Melittin-loaded Iron Oxide Nanoparticles Prevent Intracranial Arterial Dolichoectasia Development through Inhibition of Macrophage-mediated Inflammation. *Int J Biol Sci*. 2021;17(14):3818–3836. doi:10.7150/ijbs.60588
12. El-Seedi HR, Eid N, Abd El-Wahed AA, et al. Honey Bee Products: preclinical and Clinical Studies of Their Anti-inflammatory and Immunomodulatory Properties. *Front Nutr*. 2022;8:761267. doi:10.3389/fnut.2021.761267
13. Genç Karadeniz D, Kaskatepe B, Öztürk Ş, Güvenir M. In vitro and in vivo activity of Melittin combined with imipenem and meropenem against carbapenem-resistant A. baumannii. *Future Microbiol*. 2025;20(15):997–1006. doi:10.1080/17460913.2025.2572931
14. Pereira AFM, Sani AA, Zapata TB, et al. Synergistic Antibacterial Efficacy of Melittin in Combination with Oxacillin against Methicillin-Resistant Staphylococcus aureus (MRSA). *Microorganisms*. 2023;11(12):2868. doi:10.3390/microorganisms11122868
15. Nguyen CD, Yoo J, Jeong SJ, et al. Melittin - the main component of bee venom: a promising therapeutic agent for neuroprotection through keap1/ Nrf2/HO-1 pathway activation. *Chin Med*. 2024;19(1):166. doi:10.1186/s13020-024-01020-x
16. Nguyen CD, Lee G. Neuroprotective Activity of Melittin—The Main Component of Bee Venom—Against Oxidative Stress Induced by Aβ25–35 in In Vitro and In Vivo Models. *Antioxidants*. 2021;10(11):1654. doi:10.3390/antiox10111654
17. Lee G, Bae H. Anti-Inflammatory Applications of Melittin, a Major Component of Bee Venom: detailed Mechanism of Action and Adverse Effects. *Mol Basel Switz*. 2016;21(5):616. doi:10.3390/molecules21050616
18. Ma J, Wu Y, Zou H, Wang H, Zhou M, Wang H. Acid-Responsive Aggregation of Gold Nanoparticles for the Photothermal Treatment of Bacterial Infections. *ACS Infect Dis*. 2023;9(12):2538–2547. doi:10.1021/acsinfecdis.3c00389

19. Zeng X, Tang L, Zhang W, Hong X, Xiao Y. Shape and Size Effects of Gold Nanoparticles for Tumor Photoacoustic Imaging and Photothermal Therapy Within the NIR-I and NIR-II Biowindows. *Small Weinh Bergstr Ger*. 2025;21(21):e2412296. doi:10.1002/smll.202412296
20. Zou Y, Qin C, Yang L, Li X, Zhang B, Wu X. Effect of hollow structure on solar thermal applications of Au nanodiscs. *J Mol Liq*. 2024;393:123528. doi:10.1016/j.molliq.2023.123528
21. Damani M, Desai N, Singh BP, Ningthoujam RS, Momin M, Khan T. Synthesis of hollow gold nanoparticles - impact of variables on process optimization. *J Pharm Sci*. 2022;111(10):2907–2916. doi:10.1016/j.xphs.2022.08.003
22. Zhao H, Zhao H, Tang Y, et al. Skin-permeable gold nanoparticles with modifications azelamide monoethanolamine ameliorate inflammatory skin diseases. *Biomark Res*. 2024;12(1):118. doi:10.1186/s40364-024-00663-0
23. Peilin W, Ying P, Renyuan W, et al. Size-dependent gold nanoparticles induce macrophage M2 polarization and promote intracellular clearance of Staphylococcus aureus to alleviate tissue infection. *Mater Today Bio*. 2023;21:100700. doi:10.1016/j.mtbio.2023.100700
24. Zhongwei C, Junjie Y, Yuting Z, et al. Dual enzyme-like activities of iron oxide nanoparticles and their implication for diminishing cytotoxicity. *ACS Nano*. 2012;6(5). doi:10.1021/nn300291r
25. Wang T, Hu J, Ouyang R, et al. Nature of metal-support interaction for metal catalysts on oxide supports. *Science*. 2024;386(6724):915–920. doi:10.1126/science.adp6034
26. Zhao Y, Zhang J, Zhang G, Huang H, Tan WS, Cai H. Injectable Nanocomposite Hydrogel with Synergistic Biofilm Eradication and Enhanced Re-epithelialization for Accelerated Diabetic Wound Healing. *ACS Appl Mater Interfaces*. 2024;16(50):69086–69102. doi:10.1021/acsami.4c17855
27. Liu Y, Yang X, Wu K, et al. Skin-Inspired and Self-Regulated Hydrophobic Hydrogel for Diabetic Wound Therapy. *Adv Mater Deerfield Beach Fla*. 2025;37(16):e2414989. doi:10.1002/adma.202414989
28. Zhang F, Zhang H, Wang S, et al. A dynamically phase-adaptive regulating hydrogel promotes ultrafast anti-fibrotic wound healing. *Nat Commun*. 2025;16(1):3738. doi:10.1038/s41467-025-58987-w
29. Li H, Wen H, Zhang H, et al. A multifunctional dihydromyricetin-loaded hydrogel for the sequential modulation of diabetic wound healing and glycemic control. *Burns Trauma*. 2025;13:tkaf024. doi:10.1093/burnst/tkaf024
30. Yu X, Liu H, Chen L, et al. Thermosensitive antibacterial nanocomposite hydrogel guiding macrophage polarization and bone regeneration for periodontitis treatment. *Bioact Mater*. 2026;55:376–390. doi:10.1016/j.bioactmat.2025.09.030
31. Cheng H, Wang C, Qin D, Xia Y. Galvanic replacement synthesis of metal nanostructures: bridging the gap between chemical and electrochemical approaches. *Acc Chem Res*. 2023;56(7):900–909. doi:10.1021/acs.accounts.3c00067
32. Petkova-Olsson Y, Oelschlaeger C, Ullsten H, Järnström L. Structural, microrheological and kinetic properties of a ternary silica-pluronic F127-starch thermosensitive system. *J Colloid Interface Sci*. 2018;514:459–467. doi:10.1016/j.jcis.2017.12.051
33. Zhao M, Zhu S, Zhang D, et al. Long-lasting postoperative analgesia with local anesthetic-loaded hydrogels prevent tumor recurrence via enhancing CD8+T cell infiltration. *J Nanobiotechnology*. 2023;21(1):50. doi:10.1186/s12951-023-01803-8
34. Chu TW, Ho CC, Chiu HP, et al. d-Limonene inhibits cytokines and chemokines expression by regulating NF-kappaB and STAT in HaCat cells and DNCB-induced atopic dermatitis in BALB/c mice. *Int Immunopharmacol*. 2025;148:114082. doi:10.1016/j.intimp.2025.114082
35. Kim G, Han DW, Lee JH. The cytoprotective effects of baicalein on H2O2-induced ROS by maintaining mitochondrial homeostasis and cellular tight junction in HaCaT keratinocytes. *Antioxidants*. 2023;12(4):902. doi:10.3390/antiox12040902
36. Liu S, Xin R, Zhang X, Han L. Separable Microneedle Patch Integrated with the Dictamnine-Loaded Copper MOF Nanozyme for Atopic Dermatitis Treatment. *ACS Appl Mater Interfaces*. 2025;17(18):26386–26401. doi:10.1021/acsami.5c02334
37. Xun K, Tao S, Liang Z, et al. Synergistic Theranostics of Magnetic Resonance Imaging and Photothermal Therapy of Breast Cancer Based on the Janus Nanostructures Fe3O4-Aushell-PEG. *Int J Nanomedicine*. 2021;16. doi:10.2147/IJN.S322894
38. Dileseigres AS, Prado Y, Pluchery O. How to use localized surface plasmon for monitoring the adsorption of thiol molecules on gold nanoparticles? *Nanomaterials*. 2022;12(2):292. doi:10.3390/nano12020292
39. Patel S, Kim J, Herrera M, Mukherjee A, Kabanov AV, Sahay G. Brief update on endocytosis of nanomedicines. *Adv Drug Deliv Rev*. 2019;144:90–111. doi:10.1016/j.addr.2019.08.004
40. Pala V, Rosset F, Mastorino L, et al. The central role of TH2 immune response in inflammatory dermatoses: from pathogenesis to targeted therapies. *Int J Mol Sci*. 2025;26(21):10720. doi:10.3390/ijms262110720
41. Brunello L. Atopic dermatitis. *Nat Rev Dis Primer*. 2018;4(1):2. doi:10.1038/s41572-018-0004-9
42. Indra AK. Epidermal TSLP: a trigger factor for pathogenesis of atopic dermatitis. *Expert Rev Proteomics*. 2013;10(4):309–311. doi:10.1586/14789450.2013.814881
43. Vu AT, Chen X, Xie Y, et al. Extracellular double-stranded RNA induces TSLP via an endosomal acidification- and NF-κB-dependent pathway in human keratinocytes. *J Invest Dermatol*. 2011;131(11):2205–2212. doi:10.1038/jid.2011.185
44. Bertino L, Guarneri F, Cannavò SP, Casciaro M, Pioggia G, Gangemi S. Oxidative Stress and Atopic Dermatitis. *Antioxid Basel Switz*. 2020;9(3):196. doi:10.3390/antiox9030196
45. Choi DI, Park JH, Choi JY, et al. Keratinocytes-derived reactive oxygen species play an active role to induce type 2 inflammation of the skin: a pathogenic role of reactive oxygen species at the early phase of atopic dermatitis. *Ann Dermatol*. 2021;33(1):26–36. doi:10.5021/ad.2021.33.1.26
46. Tao Y, Ju E, Ren J, Qu X. Bifunctionalized mesoporous silica-supported gold nanoparticles: intrinsic oxidase and peroxidase catalytic activities for antibacterial applications. *Adv Mater*. 2015;27(6):1097–1104. doi:10.1002/adma.201405105
47. Hulme J. Staphylococcus infection: relapsing atopic dermatitis and microbial restoration. *Antibiotics*. 2023;12(2):222. doi:10.3390/antibiotics12020222
48. Zhao Z, Zhang Y, Cheng Y, et al. Thermosensitive Nanotherapeutics for Localized Photothermal Ablation of MRSA-Infected Osteomyelitis Combined with Chemotherapy. *ACS Appl Mater Interfaces*. 2023;15(10):12842–12854. doi:10.1021/acsami.2c23312
49. Ottman N, Barrientos-Somarribas M, Fyhrquist N, et al. Microbial and transcriptional differences elucidate atopic dermatitis heterogeneity across skin sites. *Allergy*. 2021;76(4):1173–1187. doi:10.1111/all.14606
50. Gonzalez T, Biagini Myers JM, Herr AB, Khurana Hershey GK. Staphylococcal biofilms in atopic dermatitis. *Curr Allergy Asthma Rep*. 2017;17(12):81. doi:10.1007/s11882-017-0750-x
51. Eg DD, C I, C B, et al. Staphylococcus aureus and the cutaneous microbiota biofilms in the pathogenesis of atopic dermatitis. *Microorganisms*. 2019;7(9). doi:10.3390/microorganisms7090301

52. Wen Y, Li Y, Liu T, et al. Nucleoside-based hydrogel platform synergizes with photothermal effects for enhanced biofilm eradication against periodontitis. *Adv Sci*. 2025;2025:e22853. doi:10.1002/advs.202522853
53. Chen L, Liang D, Qin Y, et al. AIEgen-based photothermal nanoparticles with dual antibacterial and anti-inflammatory activities for enhanced healing of infected diabetic wounds. *Small*. 2026;2025:e10741. doi:10.1002/smll.202510741
54. Jiajia H, Xuemei L, Zhiciong D, et al. How Melittin Inserts into Cell Membrane: conformational Changes, Inter-Peptide Cooperation, and Disturbance on the Membrane. *Mol Basel Switz*. 2019;24(9). doi:10.3390/molecules24091775